

Neutral Winds and Densities at the Bottomside of the F layer from Primary and Secondary Gravity Waves from Deep Convection

Sharon L. Vadas and Han-Li. Liu

Abstract We model the primary gravity waves (GWs) excited by overshooting convective plumes in a $20^\circ \times 20^\circ$ region in central Brazil for 6 hours during the evening on 01 October, 2005. We ray trace these GWs into the thermosphere. At $z = 250$ km (near the bottomside of the F layer), the surviving GWs have horizontal wavelengths of $\lambda_H \sim 200 - 300$ km, horizontal velocity amplitudes of $u', v' \leq 15$ m/s, and neutral density perturbations of $\rho'/\bar{\rho} \leq 2\%$. We compute the thermospheric body forces, and input them into the Thermosphere-Ionosphere-Mesosphere-Electrodynamics General Circulation Model (TIME-GCM). These forces create a “mean” eastward wind perturbation at $z \sim 150$ km of $200 - 340$ m/s which lasts for ~ 3 hrs. These forces also excite large-scale secondary GWs in all directions for at least 3 hours with horizontal wavelengths of $\lambda_H \sim 4000 - 5000$ km, horizontal phase speeds of $c_H \sim 500 - 600$ m/s, and density perturbations of 5-15% at $z = 250$ km. Prior to and after sunset, the wind perturbations are eastward with $u' \sim 75 - 150$ m/s at $z = 250$ km. This occurs over the convective region, where the winds from 2 large vortices (created by the forces) converge. In other areas, the winds are west/south/northward. It is likely that these forces (and the GWs they excite) significantly affect the F region dynamo and the seeding of equatorial plasma bubbles (EPBs).

1 Introduction

GWs have been observed in the thermosphere for decades as TIDs (traveling ionospheric disturbances) [1, 2, 3, 4]. From observations and modeling, it has been

S.L. Vadas

NorthWest Research Associates, CoRA div., 3380 Mitchell Lane, Boulder, CO, USA e-mail: vasha@cora.nwra.com

H.-L. Liu

National Center for Atmospheric Research (HAO/NCAR), P.O. Box 3000, Boulder, CO, USA e-mail: liuh@ucar.edu

thought that large-scale, fast GWs are created from the aurora [1, 5, 6], while medium scale GWs with $c_H < 250 \text{ m s}^{-1}$ are created in the lower atmosphere [7, 8, 9, 10]. GWs excited by convection are frequently observed in the stratosphere (e.g., [11, 12]). If the winds are small, these GWs appear as concentric rings in airglow layers near the mesopause, a stunning confirmation of their source [13, 14, 15, 16]. These patterns can last for hours, with $\lambda_H \sim 20 - 150 \text{ km}$. Near the equator, tropical convection is the most important source of GWs which can propagate into the thermosphere.

Although models show that convective “primary” GWs can propagate to the upper mesosphere and break [17, 18], some convective GWs with large vertical wavelengths λ_z and initially small amplitudes can propagate into the thermosphere [19, 20]. Primary GWs with $\lambda_H \geq 100 \text{ km}$ and $c_H \geq 200 \text{ m/s}$ can propagate to $z = 200 - 300 \text{ km}$ before dissipating [20]. Less energetic GWs dissipate at $z \sim 110 - 220 \text{ km}$, creating horizontal thermospheric body forces [19, 21]. A single convective plume creates an acceleration of $\sim 1 \text{ m/s}^2$ and “mean” winds of $\sim 400 \text{ m/s}$ at $z \sim 180 \text{ km}$, and excites large-scale “secondary” GWs with $\lambda_H \sim 2200 \text{ km}$ and $c_H \sim 500 \text{ m/s}$ which propagate up to at least $z \sim 420 \text{ km}$ [21]. A recent ray trace study showed that the TIDs observed at the bottomside of the F layer near Wallops Island, USA (75.47° W and 37.95° N) were secondary GWs excited by the thermospheric body forces created by deep convection in Tropical Storm Noel [22].

Models show that GWs at the bottomside of the F layer can seed equatorial spread F (ESF) and EPBs through the Rayleigh-Taylor (RT) instability [23, 24, 25]. Radar results have correlated wave structure in the bottomside ionosphere with the separations of plumes that develop thereafter [26, 27]. One study found wavelengths of 200-400 km [28]. Another study showed a linear relationship between the wavelengths of the GWs observed near the mesopause with EPB spacings [29]. [30] found a median spacing of $\sim 380 \text{ km}$ for periodic equatorial irregularities. A recent study found that the spacings between multiple, periodic EPBs (100 to 800 km) agreed well with the spectrum of secondary GWs from the Wallops Island study [31].

At the dip (magnetic) equator, GW seeding altitudes are $z = 200 - 300 \text{ km}$. These altitudes can be lower farther from the dip equator where the field lines are lower, if electric field perturbations are created by the GWs which then map to the magnetic equator and create the RT instability [32]. GW perturbations must be aligned with the magnetic field in order for the field-integrated perturbations to be sufficiently large [33]. When ESF occurs, it is nearly always observed after sunset, when the ionosphere descends. During this descent, spatial resonance can occur with approximately eastward propagating GWs, since plasma drifts in the eastward direction [34]. An eastward neutral wind is required to drive the F layer dynamo which creates the pre-sunset prereversal enhancement electric field (PRE)/vertical drift [35, 36], although a recent study questions the need for a strong PRE in generating ESF [37].

Although [21] calculated the primary and secondary GWs that result from a single convective plume, convection generally lasts for hours and involves tens to hundreds of plumes. The purpose of this paper is to calculate the primary and secondary GWs near the bottomside of the F layer that result from 6 hours of deep convection.

2 Primary GWs from Convective Overshoot

Convective sources of gravity waves can be described equivalently as heating or momentum sources, as these sources are coupled through the vertical momentum equation. Many linear models of GW excitation from convection have been developed [38, 39, 40, 41, 42]. Here, we use an analytic, linear, Boussinesq model which describes the excitation of GWs from a convective plume envelope with diameter \mathcal{D}_H via an upward acceleration of air [43]. This model neglects moisture processes, and assumes that the air above the tropopause is stationary within the frame of the mean horizontal wind at the tropopause until a convective plume overshoots the tropopause and pushes the stratospheric air upwards. It solves the linear solutions in a locally unshered environment with a constant buoyancy frequency.

GOES-12 satellite images covering 45 – 65° W and 0 – 20° S in central Brazil were available every 30 minutes during the 6 hour period from 18:22-23:53 UT on 01 October 2005 (e.g. [44]). Since the local time (LT) is $LT=UT-3$ hrs, this includes sunset at ~ 2230 UT. Deep convection peaked at 19-22 UT, and weakened rapidly after 23 UT. Using balloon soundings, the tropopause temperature was determined to be $\sim 209^\circ\text{K}$. All plumes cooler than this temperature likely underwent convective overshoot (i.e., punched into the stratosphere where the temperature increases), and therefore were identified as generating GWs. 136 convective objects are identified; each is classified as a single convective plume, a convective cluster containing 2 or more tightly-clumped convective plumes, or a convective complex with 2 or more

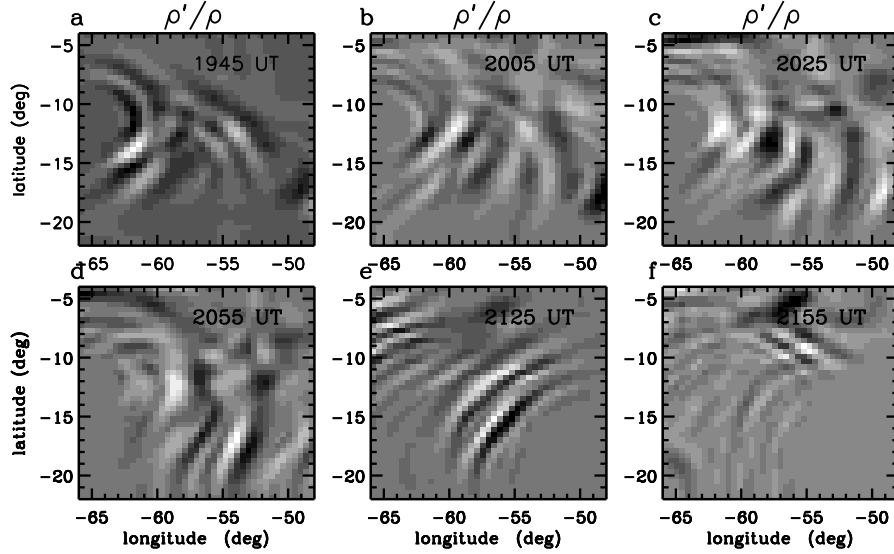


Fig. 1 Primary GW density perturbations, $\rho'/\bar{\rho}$, at $z = 250$ km from ray tracing. a)-f): 1945, 2005, 2025, 2055, 2125, and 2155 UT, respectively. Maximum positive (negative) values are white (black). The maximum values of $|\rho'/\bar{\rho}|$ are (a-c): 2, 2, and 1%. (d-f): 2, 2, and 0.3%.

less-tightly-clumped convective plumes. The average plume diameter in each object ranges from $\mathcal{D}_H = 5$ to 20 km. The plume updraft velocities, w_{pl} , are estimated from Convective Available Potential Energy (CAPE) maps, and range from $w_{\text{pl}} \simeq 0$ to 63 m/s. Because the primary and secondary GW amplitudes are proportional to w_{pl} and w_{pl}^2 , respectively, we only simulate those objects with $w_{\text{pl}} \geq 10$ m/s here. Examples of primary GW spectra excited by plumes and clusters are shown in [44]. Complexes are defined as 4 plumes at the corners of a square, with adjacent plume centers separated by $4.5\mathcal{D}_H$.

The primary GWs are ray traced into the upper atmosphere using an anelastic GW formulation [45]. The wind and temperatures are determined from balloon soundings, meteor winds, and the TIME-GCM [44]. The GW parameters are saved in a 4D box with grid spacings of $50 \text{ km} \times 50 \text{ km} \times 4 \text{ km} \times 10 \text{ min}$ in x , y , z , and t . The GW fields (such as the velocity perturbations (u', v', w') and density perturbations ρ') are then reconstructed [43]. We now also include the effects of parameterized wave breaking from self and wave-wave interactions via the use of Lindzen's saturation condition [46], as these effects are now known to be important in the thermosphere for large-amplitude waves [47, 48]. Without this effect, the non-dimensional wave amplitudes in this study would have been unrealistically large, $\sim 5 - 20$, because of the multiple clusters with large updraft velocities that occurred on this day. Including this effect decreases the altitude where the thermospheric body forces are maximum. We include this effect by ray tracing the GWs from each convective object, reconstructing the GW solution, and calculating the sum of the non-dimensional amplitude squared, A^2 , in each (x, y, z, t) bin from all convective objects. We then run the ray trace model for all convective objects again, and reduce the amplitude of each GW which enters a bin with $A > 1$ to ensure that $A = 1$ [49]. This also has the effect of altering the background flow via the deposition of momentum.

Fig. 2 Vector plot of the primary GW horizontal velocity perturbations at 1945 UT and $z = 250$ km from ray tracing. The maximum values of $|u'|$, $|v'|$, and $|w'|$ on this slice are 14, 7, and 12 m/s, respectively, where u' , v' , and w' denote the GW zonal, meridional and vertical velocity perturbations in geographic coordinates.

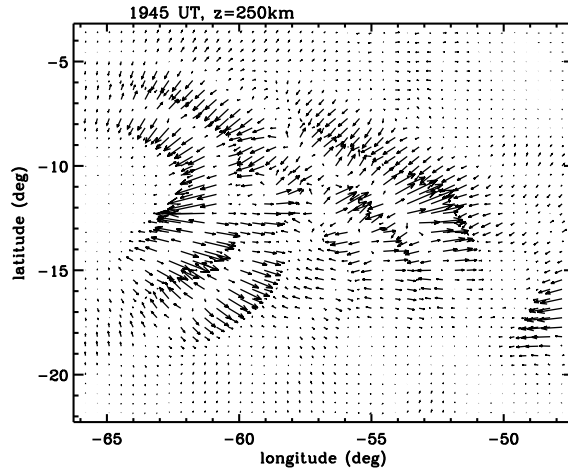


Fig. 1 shows the primary GW density perturbations at $z = 250$ km, ρ' , divided by the neutral background density $\bar{\rho}$. Lines of propagating GWs are seen. This is in contrast to $z = 150$ km, which shows mostly partial concentric rings (not shown). This difference occurs because of wind and dissipative filtering. The GWs propagate in a direction perpendicular to the phase lines, which in general is east and south-eastward. A GW's horizontal wavelength, λ_H , is the perpendicular distance between the white (or black) contour lines. From 1945 to 2155 UT, λ_H decreases from ~ 300 to 200 km.

The horizontal velocity perturbations of the primary GWs are shown at 1945 UT and $z = 250$ km in Fig. 2. The horizontal and vertical velocity perturbations, (u', v', w') , are as large as 10 – 15 m/s. These values are typical of other times. Note that w' is comparable to u', v' because the primary GW intrinsic frequency, ω_{tr} , is nearly equal to the buoyancy frequency.

3 Thermospheric Body Forces from Primary GW Dissipation

We determine the body forces which accompany primary GW dissipation and/or saturation in the thermosphere by computing the vertical divergences of the zonal and meridional momentum fluxes (per unit mass). The zonal and meridional components of the body force in geographic coordinates are

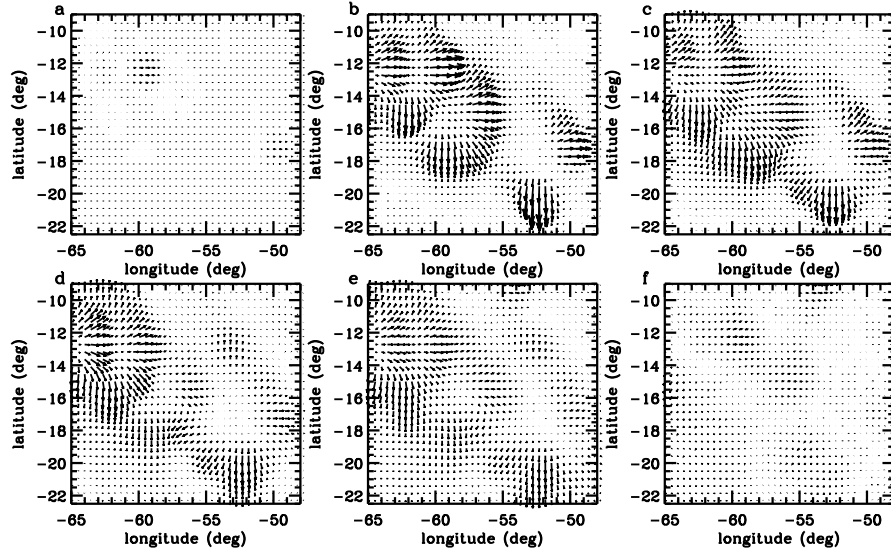


Fig. 3 a)-f): Vector plot of F_x and F_y from Eq. (1) (calculated from the ray trace solutions) every 30 minutes from 1855 to 2125 UT at $z = 152$ km. All panels are normalized by the same factor. The largest forces are $F_x = 0.68$ m/s² and $F_y = 0.83$ m/s² in b).

$$F_x = -\frac{1}{\bar{\rho}} \frac{\partial(\bar{\rho} \overline{u'w'^*})}{\partial z}, \quad F_y = -\frac{1}{\bar{\rho}} \frac{\partial(\bar{\rho} \overline{v'w'^*})}{\partial z}, \quad (1)$$

respectively [50]. Here, overlines denote averages over 1-2 wave periods and wavelengths, and * denotes the complex conjugate. If the GWs are not dissipating or saturating, $(\bar{\rho} \overline{u'w'^*})$ and $(\bar{\rho} \overline{v'w'^*})$ are constant with altitude, so that $F_x = F_y = 0$.

Because the TIME-GCM includes a GW parameterization scheme up to $z = 120$ km, we smoothly zero our body forces below 120 km in order to avoid double counting the GW effects. We choose a smoothing range of $\delta = 20$ km. For altitudes below $z_i = 100$ km, we set the body forces equal to zero. For altitudes between z_i and $z_i + \delta$, we multiply the body forces by

$$1 - \cos^2[\pi(z - z_i)/(2\delta)]. \quad (2)$$

We find that the largest value of F_x is eastward, $F_x = 0.83 \text{ m/s}^2$, and occurs at 60°W , 12°S , $z = 152$ km, and 1915 UT. The largest value of F_y is southward, $F_y = -0.89 \text{ m/s}^2$, and occurs at 53°W , 20°S , $z = 164$ km, and 1925 UT. These accelerations are consistent with previous results from a single convective plume [21]. However, the altitude of the thermospheric body force is lower here by $\sim 30 - 40$ km because of wave saturation.

Fig. 3 shows horizontal slices of (F_x, F_y) at $z = 150$ km. The strongest accelerations last for only 2 hours, from 19 to 21 UT, and are east, north, and southward. The accelerations are patchy and variable because of constructive and destructive interference between GWs from different convective objects. They have partial ring shapes because the GW phase lines are partial rings at this altitude.

GWs moving against the background wind propagate to higher altitudes in the thermosphere [51]. Those primary GWs which dissipate at $z = 150$ km are propagating in a direction which is opposite to the background wind direction 1 to 2 neutral density scale heights below $z = 150$ km (i.e., at $z \sim 120 - 130$ km) [21]. The dominant winds which filter the GWs in the lower thermosphere are semidiurnal and diurnal tides, which change on time scales of 6-12 hours. This is why the body forces in Fig. 3 are directed in a similar direction from 19 to 21 UT.

4 Generated Neutral Mean Winds and Secondary Gravity Waves

Thermospheric body forces excite secondary GWs and create “mean” neutral winds [21, 52, 53]. Because the spatial variability of the forces in Fig. 3 are $1 - 5^\circ$, we expect the secondary GWs to have horizontal wavelengths of $\lambda_H \sim 100 - 5000$ km, with a peak at $\lambda_H \sim 200 - 500$ km. (Note that the secondary GWs at the bottomside of the F layer in the Wallops Island study had $\lambda_H \sim 100 - 2000$ km, and peaked at $\lambda_H \sim 100 - 300$ km [22].) We insert F_x and F_y from Eq. (1) (as a function of x, y, z, t) into the high resolution TIME-GCM. Because of the 2.5° horizontal grid spacing of this model, however, GWs with $\lambda_H < 2000$ km are not resolvable [21]. We calculate the difference between this “perturbed” solution and the “unperturbed”

high resolution TIME-GCM solution (i.e., with no thermospheric body forces). We show the perturbed minus the unperturbed TIME-GCM solutions in Figs. 4-6.

Fig. 4 shows the neutral density perturbations of the excited secondary GWs that are resolved by the TIME-GCM (i.e., having $\lambda_H \geq 2000$ km) at $z = 250$ km. There is a density decrease of 8-12% over central and western Brazil which moves southward in time. There is also a density enhancement of 7-9% over eastern Brazil which moves southeastward in time. These occur because 1) a density decrease is created near the back-half of a body force at $z \sim 150$ km as fluid is pushed away from this region, and 2) a density enhancement is created near the front-half of a body force as fluid is pushed into a region containing existing fluid. The density perturbation amplitudes are smaller after 24 UT because the body forces are weaker then (see Fig. 3). Co-aligned with the density enhancement is a density decrease (nearer to the south pole) which also moves southeastward in time. These constitute the \pm phases of an excited large-scale secondary GW with $c_H \sim 500 - 600$ m/s and $\lambda_H \sim 4000 - 5000$ km. There are also large-scale secondary GWs which move north

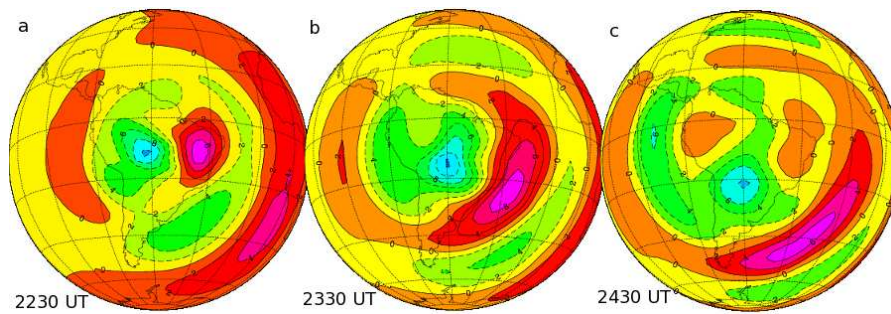


Fig. 4 Neutral density perturbations of the secondary GWs at $z = 250$ km from the TIME-GCM. (a-c) show 2230, 2330, and 2430 UT, respectively. Green (purple) colors show negative (positive) perturbations. Minimum and maximum perturbation amplitudes are a): -10 and 7%. b): -12 and 9%. c): -8 and 7%. The latitude and longitude lines on Earth are separated by 20° .

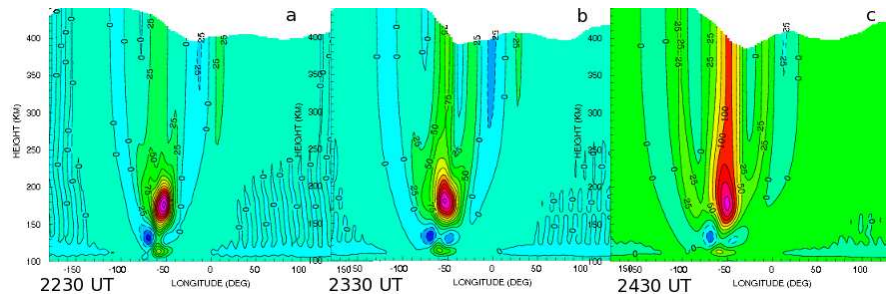


Fig. 5 Neutral zonal velocity perturbations at 14° S from the TIME-GCM. (a-c) show 2230, 2330, and 2430 UT, respectively. Green (purple) colors show negative (positive) perturbations. Minimum and maximum amplitudes are a): -85 and 340 m/s. b): -70 and 280 m/s. c): -60 and 185 m/s.

and westward in time, although their amplitudes are significantly smaller than the southeastward GWs before 24 UT.

The result that the westward and northward GWs have significantly smaller amplitudes before 24 UT differs from previous results; [21] found that the secondary GWs have similar amplitudes in and opposite to the force direction. If the background winds are small, secondary GWs excited by horizontal body forces have equal amplitudes in and against the force direction (for the same intrinsic frequency ω_{I_r}) in the intrinsic reference frame [53, 54]. In [21], the “mean” winds and secondary GWs were created at the same time. Therefore, the background winds were relatively small at the excitation time. This is not the case prior to 24 UT here. Fig. 5 shows the zonal wind perturbations (induced “mean” plus secondary GWs) at 14° S. The induced zonal mean wind is eastward from $z \sim 130$ to 230 km over a zonal extent of ~ 2000 km, with a maximum value of ~ 340 m/s at 2230 UT. There is also a large southward “mean” component (not shown). Therefore, before 24 UT, the secondary GWs are excited in a large southeastward wind created by previous thermospheric body forces. Because deep convection weakens rapidly after 2300 UT, the induced mean winds from the forces are weak after 24 UT (see Fig. 5).

We now discuss the influence of the background wind on the secondary GW amplitudes at $z = 250$ km. The ground based frequency (ω_r) of a GW is

$$\omega_r = \omega_{I_r} + kU + lV, \quad (3)$$

where U and V are the zonal and meridional background winds (which include the tides and the mean winds induced by the body forces), and (k, l, m) is the wavevector. We consider an eastward body force. If the background wind is eastward at the excitation altitude, ω_r is larger (smaller) in the forcing region for secondary GWs

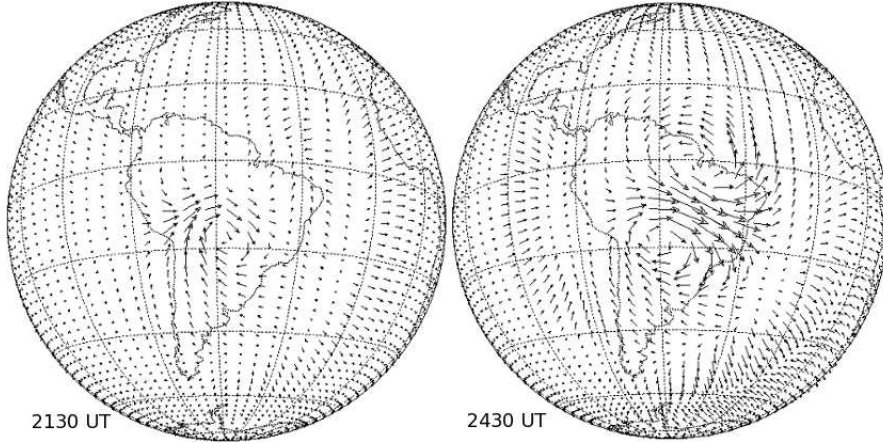


Fig. 6 Horizontal velocity perturbations of the secondary GWs at $z = 250$ km from the TIME-GCM. a): 2130 UT. b): 2430 UT. Max perturbation amplitudes are a): 75 m/s. b): 150 m/s. The latitude and longitude lines on Earth are separated by 20° .

(with the same ω_{I_r}) propagating eastward (westward). These east and westward GWs have the same initial amplitudes. Above the forcing region (at $z \geq 200$ km), U and V are much smaller, because the induced mean winds are small. Since ω_r is approximately constant along a GW's ray path, ω_{I_r} is therefore larger (smaller) at $z \geq 200$ km for the secondary GW propagating east (west), using Eq. (3). From the dispersion relation, λ_z is larger (smaller) for a GW with a larger (smaller) ω_{I_r} . Since a GW with smaller (larger) λ_z and ω_{I_r} dissipate at a lower (higher) altitude [20], the eastward GW amplitude is larger than the westward GW amplitude at $z = 250$ km prior to 24 UT. After 24 UT, the background wind at $z = 150$ km is much smaller because the body forces are weaker (see Fig. 3). This causes ω_r to be approximately equal for these same secondary GWs, causing their amplitudes to be nearly the same at $z = 250$ km since they are dissipating similarly with altitude.

Fig. 5 also shows that some secondary GWs propagate up to at least $z \sim 410 - 450$ km. Additionally, the amplitude difference between the eastward and westward secondary GWs prior to 24 UT does not occur at 2430 UT, in agreement with Fig. 4.

Fig. 6 shows the horizontal velocity perturbations at $z = 250$ km prior to and after sunset. At this altitude, the “mean” wind created by the body forces is small (see Fig. 5). Therefore, these are primarily secondary GWs perturbations. 2 large vortices swirl the neutral fluid in opposite directions above the convective region. Persistent east and southeastward motions of $u' \sim 75 - 150$ m/s occur where these vortices converge. The perturbations last for at least 3 hrs because convection occurs for ~ 4 hours this night; as secondary GWs propagate upward from the forces, new secondary GWs are excited. These horizontal velocity perturbations are much larger than that of the primary GWs at this altitude (see Fig. 2).

5 Conclusions

In this paper, we calculated the primary GWs excited by 6 hrs of deep convection on 01 October, 2005, in central Brazil. We then calculated the large-scale secondary GWs excited by the thermospheric body forces created by the dissipation of these primary GWs. We found that both primary and secondary GWs are present at the bottomside of the F layer (assumed to be at $z = 250$ km): 1) the primary GWs have $\lambda_H \sim 200 - 300$ km, $u', v' \sim 10 - 15$ m/s, and neutral density perturbations of 1-2%; 2) the secondary GWs resolvable by the TIME-GCM (i.e., having $\lambda_H \geq 2000$ km) have $\lambda_H \sim 4000 - 5000$ km, zonal wind perturbations of $u' \sim 75 - 150$ m/s, and neutral density perturbations of 10-15%. The velocity perturbations are eastward in central Brazil for 20° in longitude where the winds from 2 large vortices (created by the forcings) converge, with $u' \sim 75 - 150$ m/s. This occurs prior to and after sunset above the region of deep convection. Other regions had north, south, or westward velocities. Note that the eastward GW velocities were larger than the background tidal winds.

The pre-sunset eastward neutral winds are necessary for driving the F layer dynamo which creates the PRE. The eastward wind component of the tides were weak

at and before 2100 UT at F-layer altitudes, and became eastward thereafter, with amplitudes of ~ 100 m/s by 23-24 UT [21, 32]. Thus, the tidal wind amplitude is smaller than the eastward velocity perturbation created by the body force prior to sunset ($u' \sim 75$ m/s from Fig. 6). Additionally, the tidal wind varies spatially over tens of degrees, whereas the perturbation velocities vary over horizontal scales of 500 – 1000 km. Since only localized regions have eastward wind perturbations, the “mean” winds and large-scale secondary GWs induced by thermospheric body forces likely significantly influence the F layer dynamo and EPB seeding.

Acknowledgements SLV would like to thank Pete Stamus for the convective plume/cluster parameters, Fernando Sao Sabbas for the GOES-12 satellite images, and Ben Foster for implementing the body forces into the TIME-GCM. SLV was supported by NASA contract NNH07CC81C. HLL was supported in part by NASA contract NNH07CC81C. The National Center for Atmospheric Research is sponsored by the National Science Foundation.

References

1. Hocke, K., and K. Schlegel: A review of atmospheric gravity waves and traveling ionospheric disturbances: 1982 - 1995. *Ann. Geophys.*, **14**, 917–940 (1996).
2. Oliver, W. L., Y. Otsuka, M. Sato, T. Takami, and S. Fukao: A climatology of F region gravity wave propagation over the middle and upper atmosphere radar. *Jour. Geoph. Res.*, **102**, 14,499–14,512 (1997).
3. Djuth, F.T., M.P. Sulzer, J.H. Elder, and V. B. Wickwar: High-resolution studies of atmosphere-ionosphere coupling at Arecibo Observatory, Puerto Rico. *Radio Sci.*, **32**, 2321–2344 (1997).
4. Djuth, F.T., M.P. Sulzer, S.A. Gonzales, J.D. Mathews, J.H. Elder, and R.L. Walterscheid: A continuum of gravity waves in the Arecibo thermosphere? *Geophys. Res. Lett.*, **31**, 10.1029/2003GL019376 (2004).
5. Richmond, A. D.: Gravity wave generation, propagation, and dissipation in the thermosphere. *Jour. Geoph. Res.*, **83**, 4131–4145 (1978).
6. Hickey, M. P. and K. D. Cole: A Numerical Model for Gravity Wave Dissipation in the Thermosphere: *J. Atmos. Terres. Phys.*, **50**, 689–697 (1988).
7. Georges, T.M.: HF doppler studies of traveling ionospheric disturbances. *J. Atmos. Terres. Phys.*, **30**, 735–746 (1968).
8. Waldock, J.A. and T.B. Jones: HF doppler observations of medium-scale travelling ionospheric disturbances at mid-latitudes. *J. Atmos. Terres. Phys.*, **48**, 245–260 (1986).
9. Crowley, G, T.B. Jones, and J.R. Dudeney: Comparison of short period TID morphologies in Antarctica during geomagnetically quiet and active intervals. *J. Atmos. Terres. Phys.*, **49**, 1155–1162 (1987).
10. Ogawa, T, K. Igarashi, K. Aikyo, and H. Maeno: NNSS Satellite observations of medium-scale traveling ionospheric disturbances at southern high-latitudes. *J. Geomag. Geoelectr.*, **39**, 709–721 (1987).
11. L. Pfister, K. R. Chan, T. P. Bui, S. Bowen, M. Legg, B. Gary, K. Kelly, M. Proffitt, and W. Starr: Gravity waves generated by a tropical cyclone during the STEP tropical field program: A case study. *Jour. Geoph. Res.*, **98**, 8611–8638 (1993).
12. E. M. Dewan, R. H. Picard, R. R. O’Neil, H. A. Gardiner, J. Gibson, J. D. Mill, E. Richards, M. Kendra, and W. O. Gallery: MSX satellite observations of thunderstorm-generated gravity waves in mid-wave infrared images of the upper stratosphere. *Geophys. Res. Lett.*, **25** 939–942 (1998).

13. M. J. Taylor and M. A. Hapgood: Identification of a thunderstorm as a source of short period gravity waves in the upper atmospheric nightglow emissions. *Planet. Space Sci.*, **36**, 975–985 (1988).
14. D. D. Sentman, E. M. Wescott, R. H. Picard, J. R. Winick, H. C. Stenbaek-Nielsen, E. M. Dewan, D. R. Moudry, F. T. Sao Sabbas, M. J. Heavner, and J. Morrill: Simultaneous observations of mesospheric gravity waves and sprites generated by a midwestern thunderstorm. *J. Atmos. Solar Terres. Phys.*, **65**, 537–550 (2003).
15. S. Suzuki, K. Shiokawa, Y. Otsuka, T. Ogawa, K. Nakamura, and T. Nakamura: A concentric gravity wave structure in the mesospheric airglow images. *Jour. Geoph. Res.*, **112**, D02102, (2007), doi:10.1029/2005JD006558.
16. J. Yue, S.L. Vadas, C.-Y. She, T. Nakamura, S. Reising, H.-Li Liu, P. Stamus, D. Krueger, W. Lyons, T. Li: Concentric gravity waves in the mesosphere generated by deep convective plumes in the lower atmosphere near Fort Collins, Colorado. *Jour. Geoph. Res.*, **114**, D06104, (2009), doi:10.1029/2008JD011244.
17. J. R. Holton and M. J. Alexander: Gravity waves in the mesosphere generated by tropospheric convection. *Tellus*, **51A-B**, 45–58 (1999).
18. T. Horinouchi, T. Nakamura, and J. Kosaka: Convectively generated mesoscale gravity waves simulated throughout the middle atmosphere. *Geophys. Res. Lett.*, **29**, (2002), doi:10.1029/2002GL016069.
19. S. L. Vadas and D. C. Fritts: Influence of solar variability on gravity wave structure and dissipation in the thermosphere from tropospheric convection. *Jour. Geoph. Res.*, **111**, A10S12, (2006), doi:10.1029/2005JA011510.
20. S.L. Vadas: Horizontal and vertical propagation and dissipation of gravity waves in the thermosphere from lower atmospheric and thermospheric sources. *Jour. Geoph. Res.*, **112**, (2007) doi:10.1029/2006JA011845.
21. S.L. Vadas and H.-L. Liu: The generation of large-scale gravity waves and neutral winds in the thermosphere from the dissipation of convectively-generated gravity waves. *Jour. Geoph. Res.*, **114**, A10310, (2009), doi:10.1029/2009JA014108.
22. S.L. Vadas and G. Crowley: Sources of the traveling ionospheric disturbances observed by the ionospheric TIDDBIT sounder near Wallops Island on October 30, 2007. *Jour. Geoph. Res.*, in press, <http://www.agu.org/journals/ja/papersinpress.shtml#id2009JA015053>, (2010).
23. Kelley, M. C., M. F. Larsen, C. LaHoz, and J. P. McClure: Gravity wave initiation of equatorial spread F: A case study. *J. Geophys. Res.*, **86**, 9087 (1981).
24. Hysell, D. L., M. C. Kelley, W. E. Swartz, and R. F. Woodman: Seeding and layering of equatorial spread F. *Jour. Geoph. Res.*, **95**, 17253 (1990).
25. C.-S. Huang and M. C. Kelley: Nonlinear evolution of equatorial spread F 2. Gravity wave seeding of the Rayleigh-Taylor instability. *J. Geophys. Res.*, **101**, (A1), 293–302 (1996a).
26. R. T. Tsunoda and B. R. White: On the generation and growth of equatorial backscatter plumes: 1. Wave structure in the bottomside F layer. *J. Geophys. Res.*, **86**, 3610 (1981).
27. D. Hysell, M. Larsen, C. Swenson, A. Barjatya, T. Wheeler, T. Bullett, M. Sarango, and R. Woodman: Rocket and radar investigation of background electrodynamic and bottom-type scattering layers at the onset of equatorial spread F. *Ann. Geophys.*, **24**, (5), 1387–1400 (2006).
28. E. S. Miller, J. J. Makela, K. M. Groves, M. C. Kelley, and R. T. Tsunoda: Coordinated Study of Coherent Radar Backscatter and Optical Airglow Depletions in the Central Pacific. *J. Geophys. Res.*, in press, (2010).
29. H. Takahashi, M. J. Taylor, P.-D. Pautet, A. F. Medeiros, D. Gobbi, C. M. Wrasse, J. Fechine, M. A. Abdu, I. S. Batista, E. Paula, J. H. A. Sobral, D. Arruda, S. L. Vadas, F. S. Sabbas, and D. C. Fritts: Simultaneous observation of ionospheric plasma bubbles and mesospheric gravity waves during the SpreadFEx Campaign. *Ann. Geophys.*, **27**, 1477–1487 (2009).
30. Rottger, J.: Wave-like structures of large-scale equatorial spread-F irregularities. *J. Atmos. Terr. Phys.*, **35** (6), 1195–1206 (1973).
31. J.J. Makela, S.L. Vadas, R. Muryanto, and G. Crowley: Periodic spacing between consecutive equatorial plasma bubbles. *Geophys. Res. Lett.*, in press (2010).

32. D.C. Fritts, S. L. Vadas, D. M. Riggan, M. A. Abdu, I. S. Batista, H. Takahashi, A. Medeiros, F. Kamalabadi, H.-L. Liu, B. J. Fejer, and M. J. Taylor: Gravity wave and tidal influences on equatorial spread F based on observations during the Spread F Experiment (SpreadFEx). *Ann. Geophys.*, **26**, 3235–3252 (2008).
33. C.-S. Huang and M. C. Kelley: Nonlinear evolution of equatorial spread-F. 4. Gravity waves, velocity shear, and day-to-day variability. *Jour. Geoph. Res.*, **101**, 24,523 (1996b).
34. M. C. Kelley. (1989). *The Earth's Ionosphere*. Academic Press, San Diego, pp 487, page 130.
35. H. Rishbeth: Polarization fields produced by winds in the equatorial F region. *Planet. Space Sci.*, **19**, 357-369, (1971).
36. M. A. Abdu, I. S. Batista, G. O. Walker, J. H. A. Sobral, N. B. Trivedi and E. R. de Paula: Equatorial ionospheric electric fields during magnetospheric disturbances: local time/longitude dependences from recent EITS campaigns. *Jour. of Atmos. Terr. Phys.*, **57** 1065–1083, (1995).
37. Tsunoda, R. T., D. M. Bubenik, S. V. Thampi, and M. Yamamoto: On large-scale wave structure and equatorial spread F without a post-sunset rise of the F layer. *Geophys. Res. Lett.*, **37**, L07105, doi:10.1029/2009GL042357 (2010).
38. Stull R.B.: Internal gravity waves generated by penetrative convection. *J. Atmos. Sci.*, **33**, 1279–1286 (1976).
39. Salby, M.L. and R.R. Garcia: Transient response to localized episodic heating in the tropics. Part 1. Excitation and short-time near-field behavior. *J. Atmos. Sci.*, **44**, 458–497 (1987).
40. Alexander, M. J., J. R. Holton, and D. R. Durran: The gravity wave response above deep convection in a squall line simulation. *J. Atmos. Sci.*, **52**, 2212–2226 (1995).
41. Walterscheid, R. L., G. Schubert, and D. G. Brinkman: Small-scale gravity waves in the upper mesosphere and lower thermosphere generated by deep tropical convection. *Jour. Geoph. Res.*, **106**, D23, 31,825–31,832 (2001).
42. Beres, J.H.: Gravity wave generation by a three-dimensional thermal forcing. *J. Atmos. Sci.*, **61**, 1805–1815 (2004).
43. S.L. Vadas and D.C Fritts: Reconstruction of the gravity wave field from convective plumes via ray tracing. *Annal. Geoph.*, **27**, 147-177 (2009).
44. S.L. Vadas, M.J. Taylor, P.-D. Pautet, P.A. Stamus, D.C. Fritts, H.-L. Liu, F.T. Sao Sabbas, V.T.Rampinelli, P. Batista, and H. Takahashi: Convection: the likely source of the medium-scale gravity waves observed in the OH airglow layer near Brasilia, Brazil, during the Spread-FEx campaign. *Annal. Geoph.*, **27**, 231–259 (2009).
45. Vadas, S. L, and D. C. Fritts: Thermospheric responses to gravity waves: Influences of increasing viscosity and thermal diffusivity. *Jour. Geoph. Res.*, **110**, D15103, doi:10.1029/2004JD005574, (2005).
46. Lindzen, R.S.: Turbulence and stress owing to gravity wave and tidal breakdown. *Jour. Geoph. Res.*, **86**, 9707-9714 (1981)
47. Yiğit, E., A.D. Aylward and A.S. Medvedev: Parameterization of the effects of vertically propagating gravity waves for thermosphere general circulation models: Sensitivity study. *Jour. Geoph. Res.*, **113**, D19106, doi:10.1029/2008JD010135 (2008).
48. Yiğit, E., A.S. Medvedev, A.D. Aylward, P. Hartogh, M.J. Harris: Modeling the effects of gravity wave momentum deposition on the general circulation above the turbopause. *Jour. Geoph. Res.*, **114**, D07101, doi:10.1029/2008JD011132 (2009).
49. Smith, S.A., D.C. Fritts, and T.E. VanZandt: Evidence for a saturated spectrum of atmospheric gravity waves. *J. Atmos. Sci.*, **44**, 1404–1410 (1987).
50. D. G. Andrews, J. R. Holton, and C. B. Leovy. (1987). *Middle atmosphere dynamics*, Academic Press, Florida.
51. D.C. Fritts and S.L. Vadas: Gravity wave penetration into the thermosphere: Sensitivity to solar cycle variations and mean winds. *Ann. Geophys.*, **26**, 3841–3861 (2008).
52. Vadas, S. L.: Compressible f-plane solutions to local body forces and heatings; Part I: Initial value and forced/heated solutions. *J. Atmos. Sci.*, submitted (2010a).
53. Vadas, S. L.: Compressible f-plane solutions to local body forces and heatings; Part II: Gravity wave, acoustic wave, and mean responses, *J. Atmos. Sci.*, submitted (2010b).
54. S. L. Vadas, D. C. Fritts, and M.J. Alexander: Mechanism for the generation of secondary waves in wave breaking regions. *J. Atmos. Sci.*, **60**, 194–214 (2003).